Effect of a steep gradient in the potential energy surface on nucleon exchange

R. T. de Souza, J. R. Huizenga, and W. U. Schröder

Department of Chemistry and Nuclear Structure Research Laboratory, University of Rochester,
Rochester, New York 14627

Mass number, atomic number, energy, and angular distributions were measured for the projectile-like fragments from the reaction $^{238}U + ^{40}Ca$ at $E_{lab} = 340$ MeV. General features of this reaction are compared to other mass asymmetric systems. Considerable attention is given to the effect of the strong static driving force of the liquid drop (with shell and proximity corrections) potential energy surface on the first and second moments of the observed charge and mass distributions, as well as on associated correlations in the measured two-dimensional probability distribution $P(A,Z)$. Comparison with an appropriate nucleon exchange transport model is made and discrepancies are discussed.

I. INTRODUCTION

The motivation for studying the damped reaction $^{238}U + ^{40}Ca$ is to examine the sensitivity of the fragment mass (A) and charge (Z) distributions to the static driving forces underlying the evolution of the reaction process. The liquid-drop potential energy surface (PES) (with shell and proximity corrections) for this system exhibits considerable differences relative to the potential energy surface for systems with comparable mass asymmetry. The PES for the $^{238}U + ^{40}Ca$ system has an unusually strong gradient in the charge degree of freedom in the vicinity of the injection point. Although the effect of a larger gradient in the PES is accounted for in nucleon transport theories through inclusion of static driving forces, such theories fail to predict quantitatively the evolution of the mass and charge degrees of freedom. To better understand the evolution of the mass and charge degrees of freedom, it is necessary to measure the joint probability distribution $P(A,Z)$ of damped reaction products so as to determine possible correlations. Only a few studies to date have simultaneously measured, with better than unit resolution, the charge (Z) and mass (A) of the projectile-like fragments. In addition, some of these previous studies examined systems in which substantial ambiguity existed in the reconstruction of the preevaporative primary mass and charge distributions from the experimentally measured distributions. However, recent investigations of the neutrons and light charged particles, evaporated from systems similar to $^{238}U + ^{40}Ca$ at comparable bombarding energies, allow a much better estimate of evaporative effects on the primary mass and charge distributions.

The system presented is part of a more comprehensive study of the role of nucleon exchange in the damping of the kinetic energy of relative motion of the two ions. The reaction $^{238}U + ^{40}Ca$ at $E_{lab} = 340$ MeV shows some differences from the behavior of systems measured previously ($^{238}U + ^{56}Fe$, $^{209}Bi + ^{56}Fe$, $^{165}Ho + ^{56}Fe$) at 8.5

MeV/nucleon. Preliminary analysis of this system[1] has already determined that significant asymmetries exist in the mass number and atomic number degrees of freedom for large energy losses (E_{loss}). Study of the influence of shell structure effects on the equilibration of the N/Z degree of freedom may lead to a better understanding of these phenomena in terms of the underlying potential energy surface governing the evolution of the system. While it is worthwhile to focus on the possible causes for the skewness of the observed nuclide distributions and the surprisingly large drift in Z towards lower atomic number, it is through a systematic comparison of the current reaction, the reaction $^{238}U + ^{40}Ca$ at a lower energy of $E_{lab} = 260$ MeV and the system $^{238}U + ^{48}Ca$ at $E_{lab} = 410$ MeV that a clearer understanding of the microscopic phenomena responsible for the dissipative features of strongly damped collisions will hopefully emerge.

In the following sections, the observed properties of the damped reaction $^{238}U + ^{40}Ca$ at $E_{lab} = 340$ MeV will be discussed in considerable detail. Section II is concerned with the experimental and data analysis procedures. The measured charge, mass, energy, and angular distributions will be presented in Sec. III, and a comparison with phenomenological and microscopic models will be discussed in Sec. IV. Conclusions for this system will be drawn in Sec. V.

II. EXPERIMENTAL AND DATA ANALYSIS PROCEDURES

A 1.2 mg/cm^2 self-supporting monoisotopic ^{238}U target was bombarded with a 340-MeV ^{40}Ca beam supplied by Lawrence Berkeley Laboratory's SuperHILAC accelerator. Four silicon surface barrier detector telescopes were used to measure the charge (Z), mass (A), energy, and angular distributions of the projectile-like reaction products. The four transmission detectors (ΔE) ranged in thickness from 8.9 μm to 13.5 μm and the depletion

depth of the stop (E) detectors was 100 μm. The time-of-flight technique was employed to measure the mass of the reaction products simultaneously with their charge and energy in telescope 1. The time-of-flight distance was 80 cm and the telescope subtended 0.25 msr in the laboratory. Telescopes 2, 3, and 4 (Z telescopes) spanned the angular range $16° < \theta_{lab} < 88°$ while telescope 1 was positioned at $\theta_{lab} = 44°$. All telescopes were protected from delta electrons by the use of 0.13 μm Ni foils and Sm-Co magnets mounted on the face of the telescopes. Two monitor detectors situated close to 0° in plane and 12° out of plane were used for normalization to Rutherford scattering and for dead-time corrections. All telescopes were calibrated with a ThC' alpha source and a precision linear pulse generator. An energy resolution of 3% full width at half-maximum (FWHM) was achieved for elastically scattered projectiles. In the element range from $Z = 10$ to $Z = 24$, a resolution of 0.4 (FWHM) in Z and 0.5 (FWHM) in A was achieved.

A standard electronics setup was used as described elsewhere.[2] The deadtime of the electronics ranged from 5–30 %. The data were recorded event by event for later off-line analysis that was performed on VAX 11/750 and VAX 8600 computers at the University of Rochester.

Figures 1 and 2 portray the resolution in Z and A, respectively, of the raw data. In Fig. 1 a two-dimensional plot of ΔE vs E for the mass telescope demonstrates the identification of the charge (Z) of the projectile-like reaction products. In Fig. 2 the typical mass resolution of the experiment is depicted by the display of a two-dimensional plot of the pseudoparameter (relatable to the mass) $A^* = Et^2$ vs E, where t is the time of flight of the reaction product. The resolution demonstrated in these plots is the typical resolution for all telescopes through the duration of the experiment.

By measuring the velocity (v) of reaction products over a fixed flight distance and rearranging the expression for the nonrelativistic energy (E) of a body, one concludes $A \propto Et^2$, where E is the stop time-of-flight telescope and t is the transit time between start and stop. Due to non-linearities and errors associated with the calibration of the time-of-flight detector, the pseudoparameter A^* and the mass number A are not identical, although $A = f(A^*) = f(Et^2)$. However, due to the superb resolution in this experiment, it is possible to remove the energy dependence in the pseudoparameter A^* through a transformation of the A^* vs E space to the A vs E space. The transformation was performed on an event-by-event basis so as to retain all possible correlations.

Determination of the atomic number of the reaction products was accomplished by transformation of ΔE-E to Z-E utilizing the theory of Braune and Schwalm.[3-5] Parameters of the theory were fitted to eight experimentally measured energy-loss curves of $\Delta E / \Delta x$ vs E for nuclei with $Z = 18, 26, 36, 54,$ and 82 and detector thickness Δx between 7.9 and 14.8 μm. The conversion procedure followed a procedure described[6] previously, except that, in this analysis, it was implemented in an event-by-event fashion.

Due to finite experimental resolution in Z and A, the intensities of the integer atomic and mass numbers were
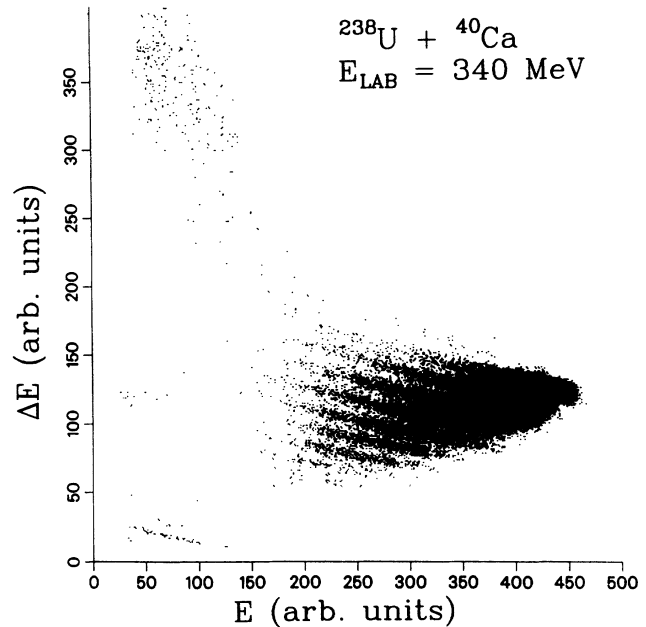

FIG. 1. Scatter plot of energy loss (ΔE) vs residual energy (E) for the projectile-like fragments demonstrates the excellent experimental resolution in Z as well as the strong drift of the projectile-like fragment towards lower Z.
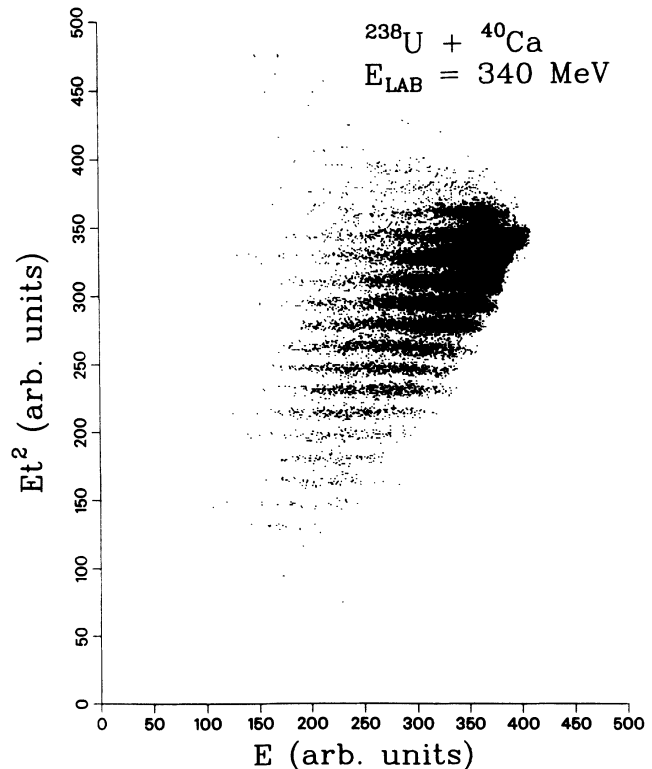

FIG. 2. Scatter plot of the pseudoparameter $A^* = Et^2$ vs energy (E) depicts the observed resolution in the mass degree of freedom.

determined by the procedure illustrated in Fig. 3. Peaks in the continuous distributions were fit with a multipeak fitting routine under the constraint of minimizing the X square. The intensity of the $A = 42$ peak is represented by the hatched area in Fig. 3. The integrals of the various peaks for the best fit correspond to the resolution-corrected Z and A distributions.

The apparent energy E_{app} measured with the stop detector was corrected for pulse height defect using the power law formula of Moulton et al.[7] The total kinetic energy loss was then calculated from two-body kinematics including the correction for isotropic neutron evaporation from the primary reaction products. The center-of-mass scattering angle $\theta_{c.m.}$ was calculated under the assumption of a binary exit channel and the resulting fully transformed data were stored in an event-by-event mode so that all correlations were maintained.

For determination of the absolute cross sections, the data were normalized to Rutherford scattering observed in the monitor detectors. The data from all Z telescopes were then summed into a $(Z, E_{loss}, \theta_{c.m.})$ array for subsequent analysis of correlations.

III. RESULTS AND DISCUSSION OF GENERAL FEATURES

A. Elastic Scattering

A study of the elastic scattering of ^{40}Ca on ^{238}U was performed to determine the quarter-point angle $\theta_{1/4}$, the strong absorption or interaction radius, and the total reaction cross section. The elastic scattering angular distribution is shown in Fig. 4 as the ratio $\sigma_{el}/\sigma_{Ruth}$ of elastic to Rutherford cross section. For angles forward of
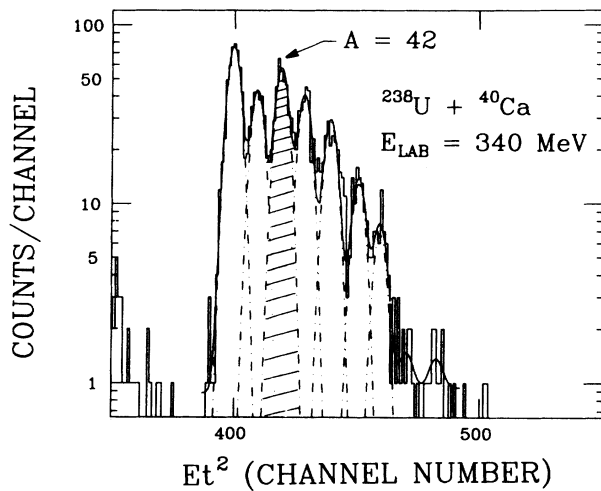

FIG. 3. Illustration of multipeak chi-square fitting technique utilized to remove the effect of the finite experimental resolution on the observed distribution. The solid curve represents the total calculated contribution of all the peaks, while the dashed curve represents the fit to individual peaks in the distribution. The intensity of the $A=42$ peak is represented by the cross-hatched area.
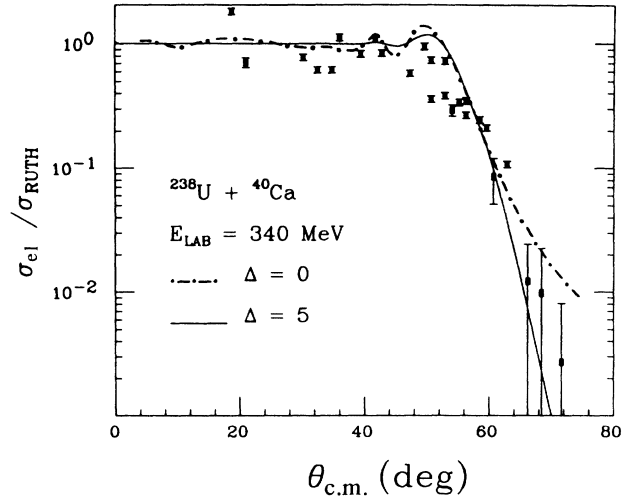

FIG. 4. Elastic scattering angular distribution in the center of mass. Experimental points represent the elastic scattering cross section relative to Rutherford cross section $(\sigma_{el}/\sigma_{Ruth})$ at a given center-of-mass scattering angle $\theta_{c.m.}$. Also shown are the result of two generalized Fresnel model calculations with $\Delta = 0$ (dashed line) and $\Delta = 5\hbar$ (solid line).

$\theta_{c.m.} \approx 52°$, Coulomb scattering dominates. For angles larger than $\theta_{c.m.} \approx 52°$ the absorption caused by the attractive nuclear force is manifested by the sharp fall-off of the distribution from unity.

The experimental data have been fitted with a generalized Fresnel model. The standard Fresnel model[8] assumes a transmission coefficient $T_l = 1$ for l waves up to a grazing angular momentum l_g and $T_l = 0$ for larger l waves. This model has been generalized by Frahn[9] to incorporate a smooth transition of the transmission coefficient from 0 to 1 under the condition that $T_l = \frac{3}{4}$ at $l = l_g$. The total reaction cross section can then be expressed as

$$\sigma = \pi \mathchar'40\mkern-9mu\chi^2 (l_g + \tfrac{1}{2})^2 \left[1 + 2\frac{\Delta l}{l_g + 1/2} + \frac{\pi^2}{3} \left[\frac{\Delta l}{l_g + 1/2} \right]^2 \right],$$

(1)

where Δl is the width of the region in angular momentum in which the transmission coefficient falls from 1 to 0. The interaction radius is then given as

$$R_{int} = \frac{\eta}{k_\infty} [1 + \csc(\tfrac{1}{2}\theta_{1/4})] .$$

(2)

The quantity η is the Sommerfeld parameter given by

$$\eta = e^2 Z_P Z_T [\mu/(2\hbar^2 E_{c.m.})]^{1/2}$$

(3)

and the parameter k_∞ is the inverse of the de Broglie wavelength. In Fig. 4 the experimental elastic scattering cross section relative to the Rutherford scattering cross section is shown as a function of $\theta_{c.m.}$. In addition, the results of theoretical calculations with two values of Δl are plotted. The dashed-dotted line represents the general-

TABLE I. Reaction parameters and results of elastic scattering for the system ^{238}U + ^{40}Ca at $E_{lab} = 340$ MeV.

E_{lab}	(340±10) MeV
$E_{c.m.}$	(291±9) MeV
$\theta_{1/4}$ (lab)	51°±0.5°
$\theta_{1/4}$ (c.m.)	58.5°
μ (reduced mass)	32.24 μ
k_∞ (wave number)	21.86 fm^{-1}
η (Coulomb parameter)	99.4
R_{int} (Fresnel)	13.85 fm
l_g (Fresnel exp$\theta_{1/4}$)	178$\hbar$
σ_R (Fresnel exp$\theta_{1/4}$)	2210 mg[a]
V_C (R_{SA})	191 MeV
$E_0 = E_{c.m.} - V_C(R_{SA})$	100 MeV
$[E_{c.m.} - V_C(R_{SA})]/\mu$	3.10 MeV/nucleon
l_{RLDM}	32$\hbar$

[a]Lower limit (see text).

ized Fresnel model with $\Delta l = 0$ and the solid line represents the case of $\Delta l = 5$. It can be seen that the generalized Fresnel model with $\Delta l = 5$ represents a fairly good description of the exponential dropoff from unity for $\theta_{c.m.} \geq 52°$. The reaction parameters and results of the elastic scattering analysis are summarized in Table I. The reported total reaction cross section of 2210 mb is a lower limit due to the energy resolution of the present experiment which allows for the inclusion of some inelastic scattering in the operational definition of elastic scattering. The total reaction cross section may therefore be slightly larger than the value extracted from the present "elastic" scattering analysis of the data.

B. Damped Reactions

In Fig. 1, the region of strongly damped events, which evolves as a distinct spectral feature from the elastic peak, is well separated in $\Delta E - E$ space from the region of fusion-fission and from the region of sequential fission of uranium-like fragments. Due to their larger atomic number the latter fragments produce much larger energy losses in the ΔE detector and smaller residual energies in the E detector. A gate was set so that the operational definition of strongly damped events includes elements with atomic number $10 < Z < 25$. It should be noted that these limits also exclude the region of very light reaction products, the presence of which is due to the strongly damped products from the auxiliary reactions ^{12}C + ^{40}Ca and ^{16}O + ^{40}Ca. Buildup of carbon deposits and oxidation of the uranium target does not, however, significantly affect the quality of the results due to the clear separation of the two processes in the Z-E space. Also included in the operational definition of a damped event is an associated energy loss greater than 20 MeV. Setting such a threshold in the definition of a "reaction" event allows separation from the elastic events.

Under the constraints of the above definition for a damped event, the secondary atomic and mass number distributions summed over energy losses greater than 20 MeV are depicted in Figs. 5 and 6, respectively. These
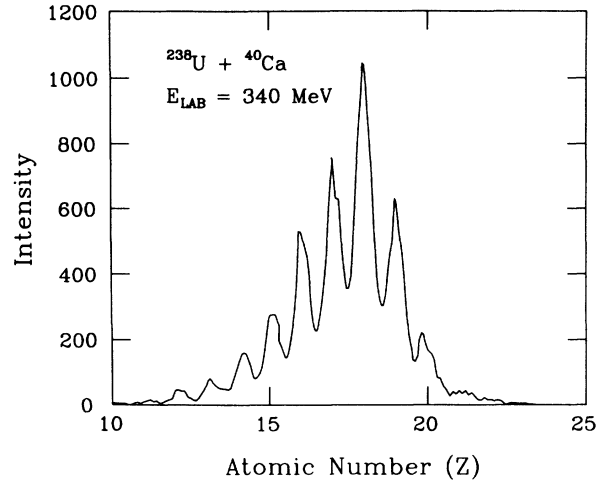

FIG. 5. Experimental atomic number (Z) distribution for all projectile-like fragments with $E_{loss} > 20$ MeV. The data were taken at $\theta_{lab} = 44°$.

data were taken at $\theta_{lab} = 44°$. The atomic number (Z) populated with the highest probability is $Z = 18$, whereas the most likely mass number of a projectile-like fragment is $A = 38$. Deviations of the A and Z distributions of the projectile-like fragments from Gaussian shapes provide clues as to the degree of departure from a parabolic shape of the underlying restoring potential responsible for the evolution of the system along the Z and A degrees of freedom. It is important to note, however, that both the mass (A) and charge (Z) distributions portrayed are secondary distributions formed by deexcitation of the primary distributions of reaction products via particle emission. All theories concerning the mechanism through which nucleon exchange between the uranium-like and calcium-like fragments mediates the dissipation of kinetic
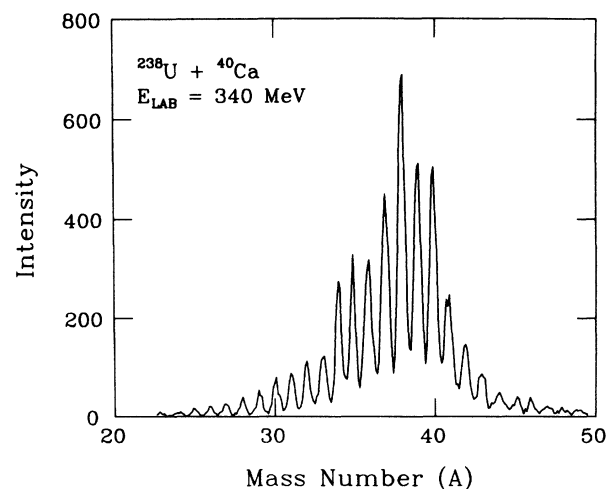

FIG. 6. Observed mass number (A) distribution for all projectile-like fragments with $E_{loss} > 20$ MeV. The data were taken at $\theta_{lab} = 44°$.

energy, relate to the primary distributions of reaction products. Thus, it is of critical importance to estimate, or preferably to measure, the degree to which the primary distributions of the reaction have been altered by particle evaporation. This point is considered in Sec. IV.

The nuclide distribution in the A-Z plane observed at a laboratory angle of 44° is shown in Fig. 7 for all reaction fragments with kinetic energy losses greater than 20 MeV. The atomic and mass numbers of the projectile (the injection point of the reaction in this plot) are $Z = 20$ and $A = 40$, and occupy a box in the upper right-hand corner of this plot designated by the reticle. Most of the secondary reaction fragments have both atomic and mass numbers that are smaller than those of the projectile, with the most intense yield for the nuclide $^{38}_{18}$Ar. The solid line represents an average of the minimum in the potential energy of the dinuclear system and the dashed line represents an average of the minimum in the β stability valley of the projectile-like fragments. Although the secondary projectile-like fragments, formed in the damped reaction process for all kinetic energy losses greater than 20 MeV, cluster around the average β-stability line, the product yield does not track with the natural isotopic abundances. The excited primary fragments on the average are more neutron rich and fall to the right of this line. This effect is much weaker than observed for the ^{238}U + ^{48}Ca reaction.[10] The most highly damped events approach the A/Z value of the minimum in the potential energy of the dinuclear system as discussed later. Despite the neutron richness of the uranium partner, the projectile ^{40}Ca is so neutron poor that no

new neutron-rich isotopes were discovered. However, sulfur isotopes with mass number up to $A = 40$ and chlorine isotopes with mass number up to $A = 42$ were observed as previously reported[11] in a study of the ^{232}Th + ^{40}Ar reaction.

In Fig. 8 the isotopic mass distributions gated on the individual elements from $Z = 11$ to $Z = 22$ are plotted for a laboratory angle of 44° and all events with kinetic energy losses greater than 20 MeV. Each major peak is labeled with the mass number to which it corresponds. Relative cross sections of some 80 nuclei are shown in Fig. 8. In the region $11 \leq Z \leq 15$ the mass distributions are relatively symmetric, however, as one progresses from $Z = 16$ (S) to $Z = 20$ (Ca) an increasing degree of asymmetry is apparent. The asymmetry is caused by a pronounced tail on the high-mass side of the distributions. For $Z = 21$ and 22 a return to a more symmetric distribution is found. Since dynamical components of the driving forces are presumably independent of charge asymmetry, perhaps the presence of the asymmetry can be ascribed to the particular shape of the potential surface in the mass degree of freedom for the Z range in question.

The complementary plot of the isobaric charge distribution (measured for the same laboratory angle and energy losses as for at Fig. 8) for a constant mass number is shown in Fig. 9 for $A = 34$–41. The markedly narrower widths of the element distributions in Fig. 9 as compared to the widths of the mass distributions in Fig. 8 clearly demonstrate the difference in the restoring forces governing the correlated evolution of the two-dimensional distribution in the A-Z plane. Narrow isobaric distributions
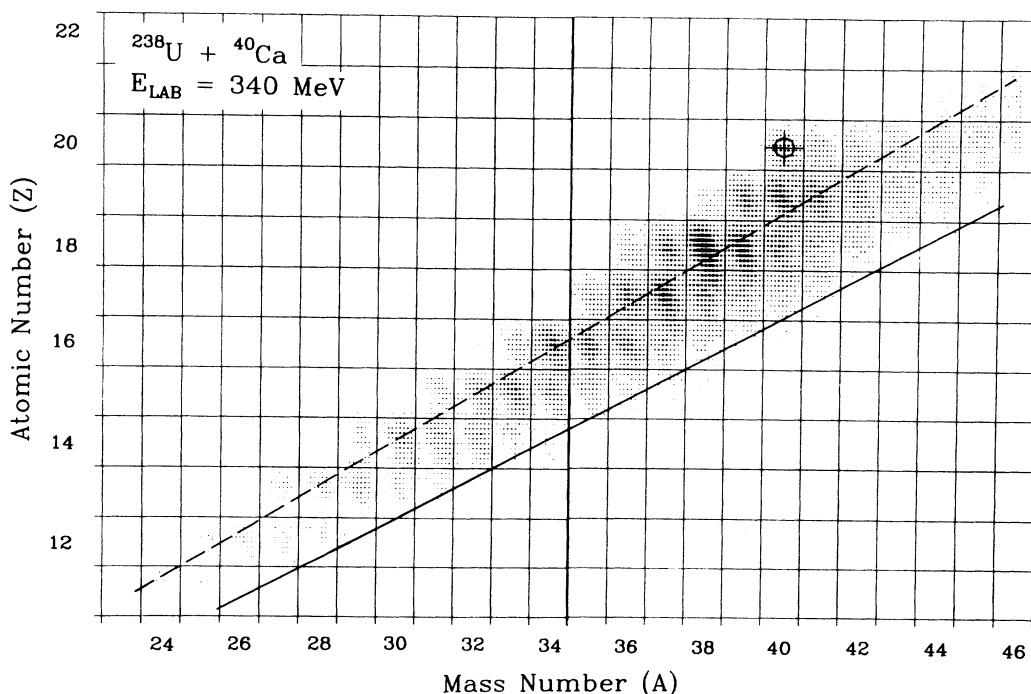

FIG. 7. Population of observed nuclides (secondary projectile-like fragments) in the (A, Z) plane represented as a density plot. The dashed line represents the beta-stability line of the projectile-like fragments. The solid line represents the minimum of the potential energy for the dinuclear system. The injection point is at $Z = 20$, $A = 40$.

(atomic number degree of freedom for fixed mass number) imply a strong restoring force to deviations from the average in the atomic number degree of freedom for fixed mass number, whereas larger widths in isotopic distributions (mass number degree of freedom for fixed atomic number) imply weaker restoring forces.

The laboratory angular distribution $d\sigma_{DC}/d\theta_{lab}$ of all damped projectile-like reaction fragments with $E_{loss} > 20$ MeV is shown in Fig. 10. The differential cross section $d\sigma_{DC}/d\theta_{lab}$ is constant within experimental error for all angles up to approximately $\theta_{lab} = 44°$ and decreases at larger angles. The exponential dropoff in cross section at
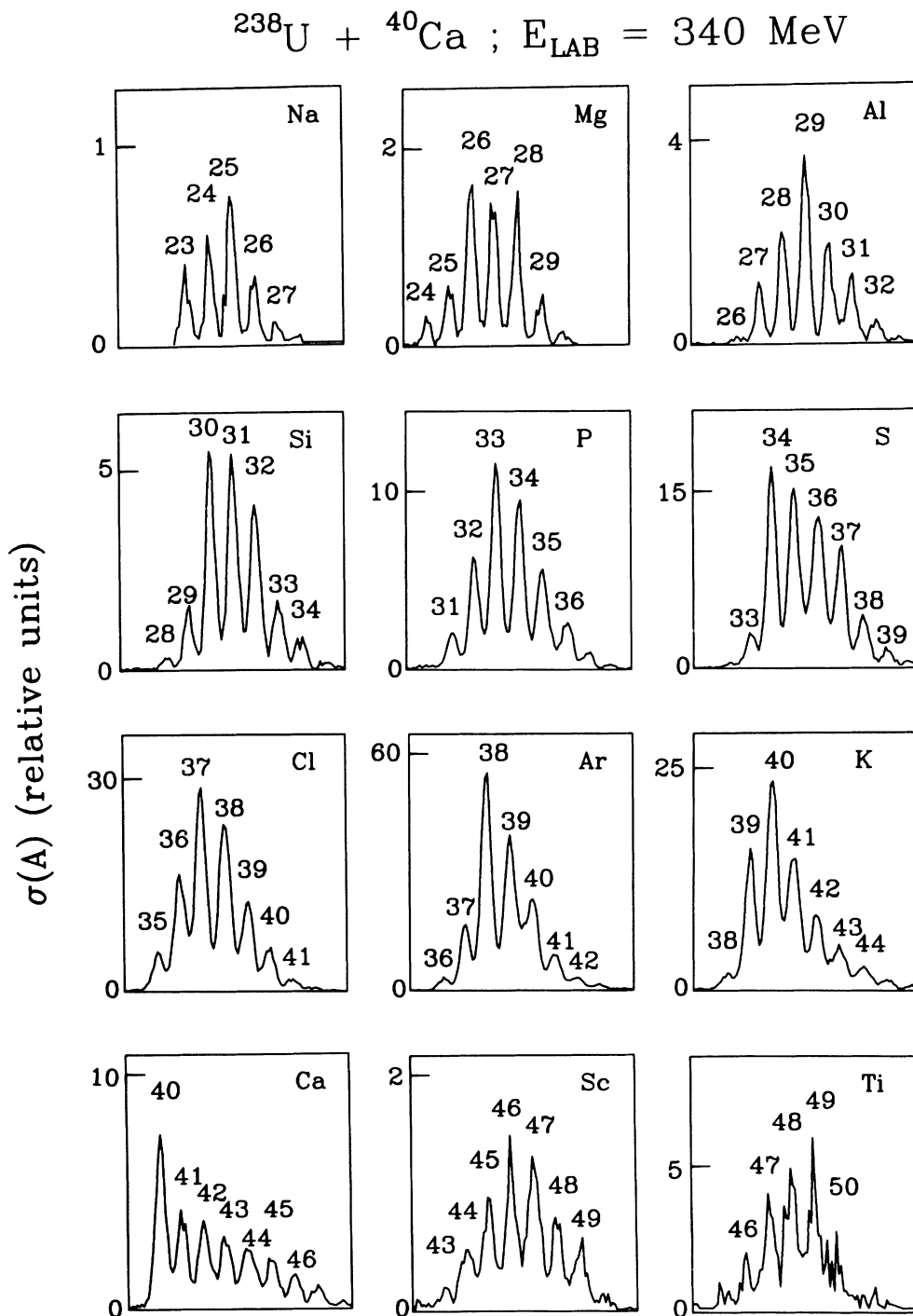

FIG. 8. Mass distributions of various elements from $Z = 11$ (Na) to $Z = 22$ (Ti) measured at $\theta_{lab} = 44°$. The peaks identifiable as the various isotopes of a particular element are labeled with their mass number. The cross sections $\sigma(A)$ are in relative units, however, in the same units for all elements.

these larger laboratory angles demonstrates that most of the reaction cross section is focused into a finite angular window in the laboratory, near and forward of the quarter-point. One interesting point is whether the angular distribution in the laboratory exhibits any special dependence on the atomic number of the reaction products. In Fig. 11 this point is considered by examining the angular distributions in the laboratory for each of the various elements produced in the reaction. The most obvious difference among the distributions is the presence of a small peak located at approximately 44° for some distributions. While all distributions for $15 < Z < 19$ have this peak, it becomes less pronounced for the lighter Z's further from the projectile. In addition, this peak does not appear in the distributions for $Z = 21$ and $Z = 22$. It will be important to recall this point later in the discussion of the diffusion contour diagram.

It has been shown in previous work that as long as the repulsive Coulomb and centrifugal forces do not overwhelm the attractive nuclear force for small internuclear separation distances, the degree of rotation of the dinuclear system prior to scission corresponds to a measure of the reaction time. Furthermore, the uncertainty in the width of the angle of rotation in the center-of-mass corresponds to an uncertainty in interaction time. In an attempt to ascertain whether the observed mass, charge,
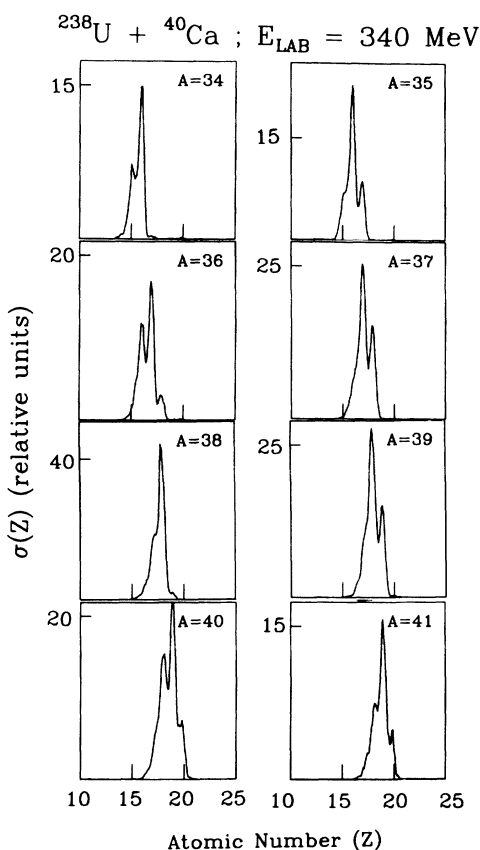
and energy distributions are limited by kinematical cutoffs, a Monte Carlo program was used to determine the correspondence between angular bins in the center of mass and the angular bins measured in the laboratory as a consequence of the finite size of the detector. It was found that the entire product distribution (Z, A, E) observed in a one-degree-wide bin in the laboratory corresponded to a (Z, A, E) distribution spread over approximately a four-degree-wide bin in the center of mass. Naturally, any restriction upon the mass, charge, or energy of the observed distribution further narrows the width of the center-of-mass angular bin. This calculation also demonstrated that kinematical cutoffs are not determining the widths of the experimentally measured distributions. Although not shown, the center-of-mass angular distributions are very similar to the respective laboratory angular distributions shown in Figs. 10 and 11. It is interesting to note that in these angular distributions, the differential cross section maintains a relatively constant value at small angles. Since the differential cross section $d\sigma_{DC}/d\theta_{c.m.} = (d\sigma_{DC}/d\Omega_{c.m.})\sin\theta$, a constant cross section at smaller angles is consistent with an orbiting type of reaction.

An instructive diagram of the dependence of the cross section on both the atomic number and the energy loss is represented as a contour plot in Fig. 12. The data in this figure have been integrated over angle. The lines represent isocontours of constant differential cross section $d^2\sigma/dE_{loss}dZ$ [in units of 10 μb/(MeV$\times Z$ unit)] with respect to E_{loss} and atomic number Z. The two striking features of this diagram are the presence of a ridge extending smoothly from the elastic peak at $Z = 20$, $E_{loss} = 0$ to smaller Z with increasing E_{loss} and the presence of a protrusion of cross section centered at $E_{loss} = 150$ MeV. There is a clear drift in charge (Z) towards lighter projectile-like fragments as energy is increasingly dissipated. The most noteworthy feature of this plot, however, is that the cross sections for Z's > 20
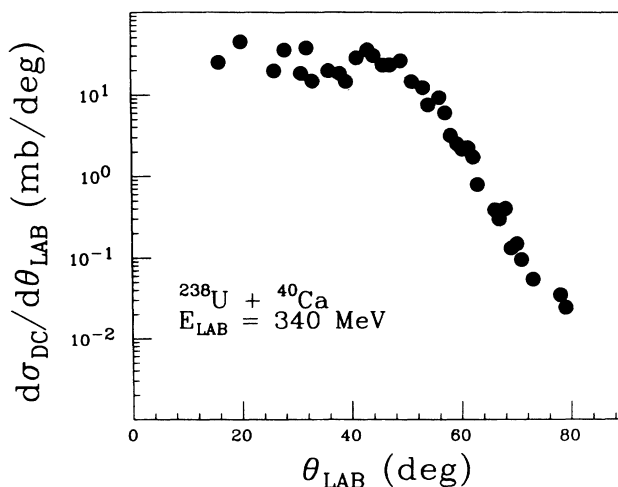

FIG. 9. Element distributions gated on mass number $(34 \leq A \leq 41)$ and measured at $\theta_{lab} = 44°$. The cross sections of all nuclides are given in relative units.

FIG. 10. Laboratory angular distribution of projectile-like fragments. The differential cross section $d\sigma_{DC}/d\theta_{lab}$ (mb/deg) is plotted as a function of θ_{lab} (deg).

which are centered at $E_{loss} = 150$ MeV do not evolve smoothly from the elastic peak but rather reside at energies which correspond to values predicted from systematics of fully relaxed events. These cross sections account

for most of the population of the elements for $Z > 20$. On consideration of the mean of the Z distribution and its width, it is difficult to completely reconcile this cross section with a conventional strongly damped picture. Relat-
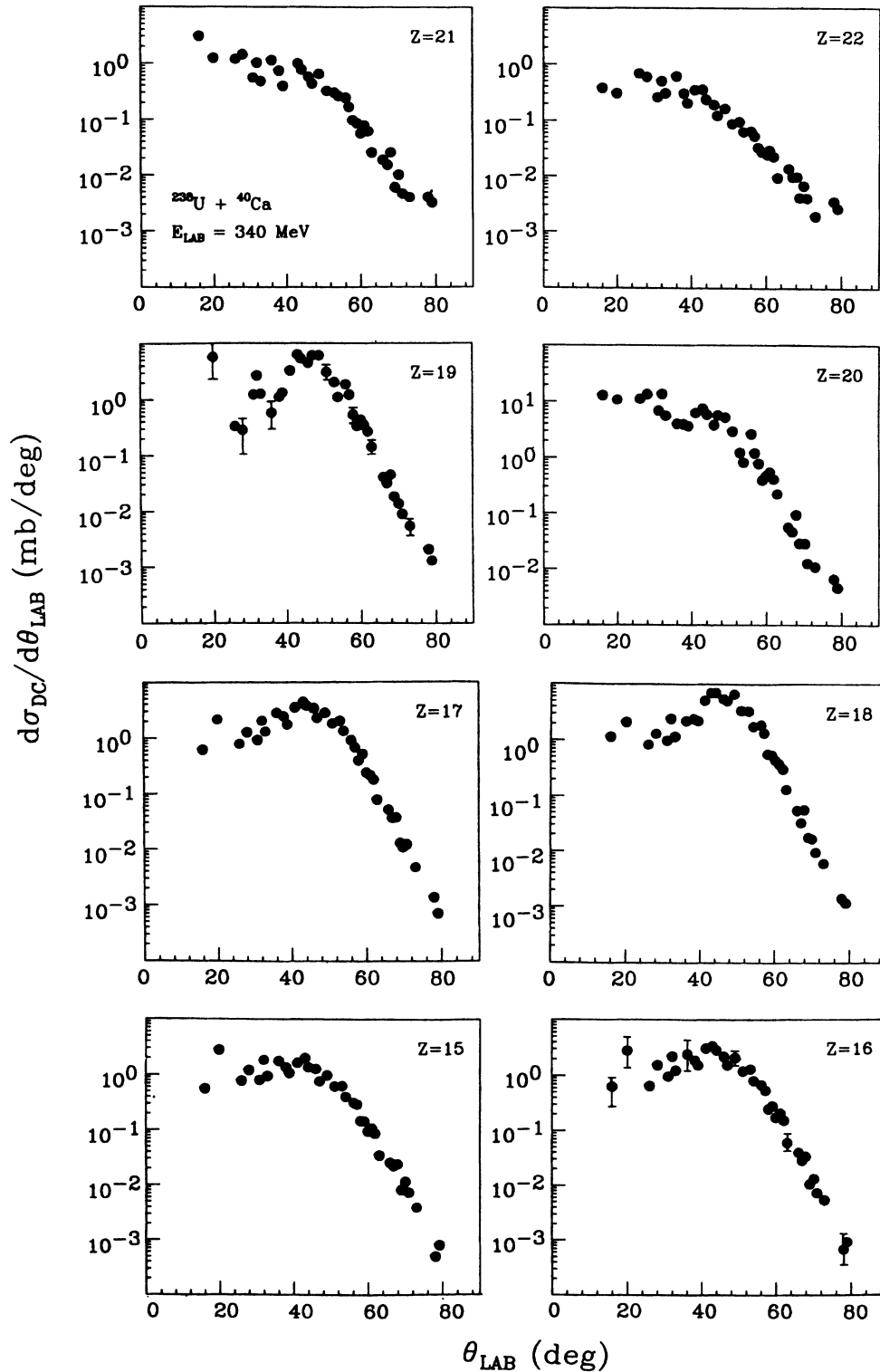
FIG. 11. Laboratory angular distribution of various elements from $Z = 16$ to $Z = 22$. The dependence of $d\sigma_{DC}/d\theta_{lab}$ (mb/deg) on laboratory scattering angle θ_{lab} (deg) is shown.
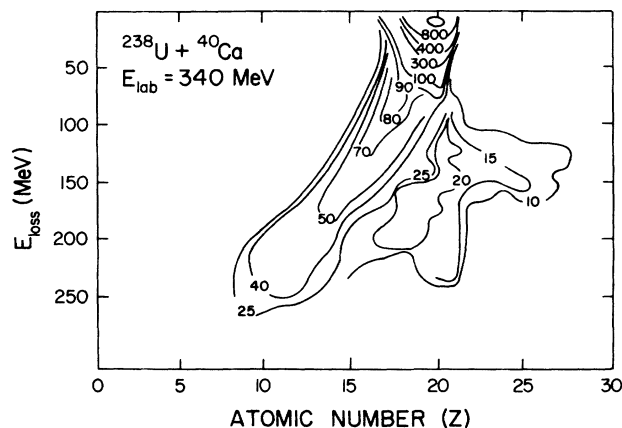
FIG. 12. Contour diagram demonstrating the dependence of the double-differential cross section $d^2\sigma/(dE_{loss}dZ)$ in units of 10 μb/(MeV$\times Z$ unit) on E_{loss} (MeV) and atomic number (Z). The strong drift towards smaller atomic number, as kinetic energy is increasingly dissipated, is clearly seen. These data cover the laboratory angular range of 15–80°.

ing the origin of this cross section to the extreme tail of the fusion-fission distribution is also difficult; perhaps its presence is due to an intermediate reaction process[12] which has characteristics of both strongly damped and fusion-fission reactions.

A more quantitative view of the population of the various elements is presented in Fig. 13. In this figure the atomic number distribution is shown for all damped events integrated over angle with $E_{loss} > 20$ MeV. The asymmetry of the raw data, first apparent in Fig. 5 for $\theta_{lab} = 44°$ is also visible in the distributions presented here, which have been corrected for the experimental resolution. In Fig. 14 the angle-integrated atomic number distributions for various energy-loss bins are shown.
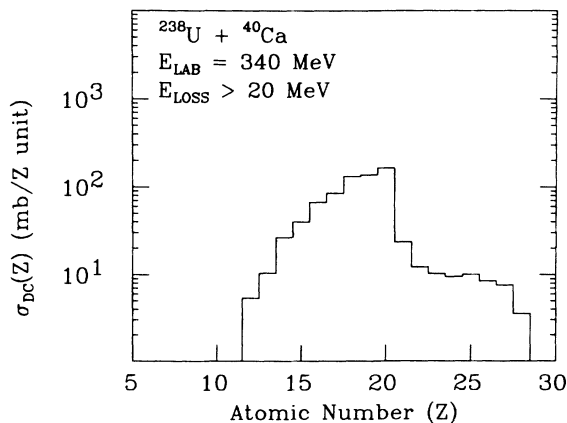

FIG. 13. Distribution of cross section of various elements is shown in this plot of $\sigma_{DC}(Z)$ in units of (mb/Z unit) vs atomic number (Z). These data cover the laboratory angular range of 15–80°.
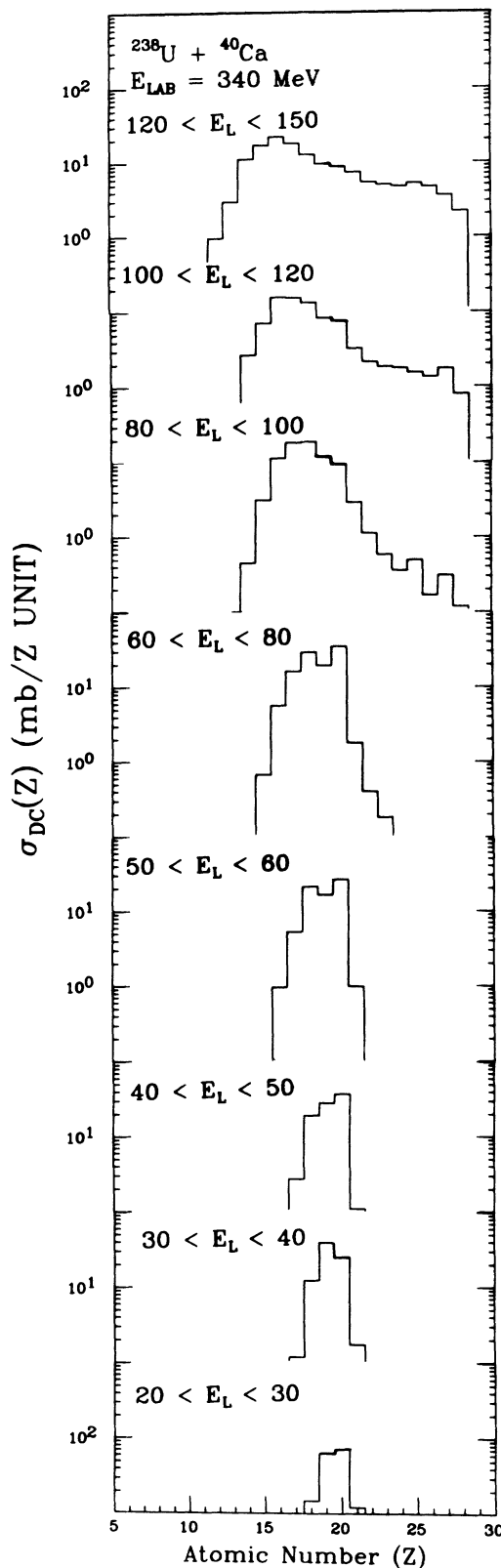

FIG. 14. The cross section σ_{DC} of the element distribution in units of (mb/Z unit) is shown for various energy loss bins. The growth in the width of the distribution for increasing damping is evident as is the motion of the centroid to lower Z values. These data cover the laboratory angular range of 15–80°.

It has been established that the amount of kinetic energy dissipated represents a relatively good measure of the duration of the collision. Thus, Fig. 14 shows the changing Z distributions as a function of increasing interaction time. The growth in the width, the motion of the centroid to lower Z values, and the degree of asymmetry are the salient features of this plot. Note that the high Z's are only populated in significant amounts for the most highly damped collisions, and that the high Z wing joins smoothly with the cross section from the ridge in Fig. 12, as it should.

The discussion of the general features of the damped collisions in this reaction is concluded with an examina-

tion of the kinetic energy distributions as a function of angle for the various elements (Figs. 15 and 16). Distributions of this kind were first used by Artukh et al.[13] to promote an orbiting picture of the reaction ^{232}Th + ^{40}Ar at $E_{lab} = 388$ MeV. In the case of the reaction ^{238}U + ^{40}Ca at $E_{lab} = 340$ MeV, the characteristics of orbiting are also clearly manifested. Examination of the $Z = 17$ column as a typical case shows that at the most forward angles and at the most backward angles the distributions are peaked at large energy loss values. At angles closer to the quarter-point angle for this reaction, however, the distributions are peaked at smaller E_{loss} values. This can be understood in terms of an orbiting
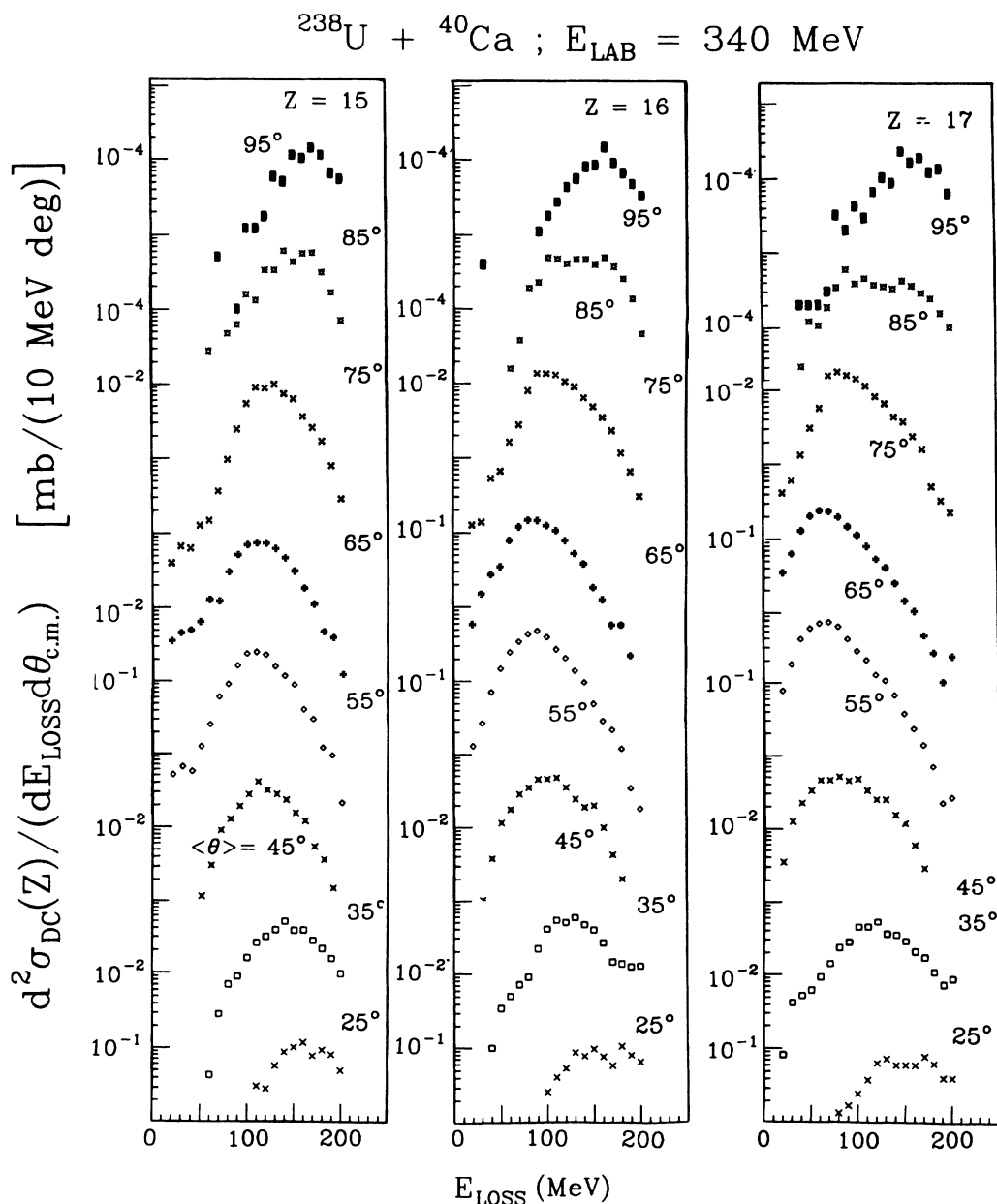

FIG. 15. Kinetic energy spectra. Dependences of the double differential $d^2\sigma/(dE_{loss}d\theta_{c.m.})$ on E_{loss} of various elements ($Z = 15,16,17$) are shown for different center-of-mass angles.

picture. Processes corresponding to small energy losses for this reaction are focused in the vicinity of the quarter-point angle. It should be noted that this "back-bending" feature of the maxima of the kinetic energy distributions becomes less pronounced as one progresses from $Z = 17$ to $Z = 15$. This is simply understood in terms of the projectile-like fragments being further removed from the projectile, requiring larger energy losses. Contamination from elastic scattering distorts the shapes of the energy spectra for $Z = 21$, especially for the smaller energy losses.

IV. EVOLUTION OF MASS, CHARGE AND THE DISSIPATION OF KINETIC ENERGY

Considerable theoretical effort has been expended to gain insight into the relationship between nucleon exchange and the dissipation of kinetic energy in a damped heavy-ion collision.[14] The various models differ with respect to the choice of collective reaction variables and the microscopic origin of the transport processes assumed. The data for this system are compared with the nucleon exchange transport theory proposed by Randrup.[15,16]
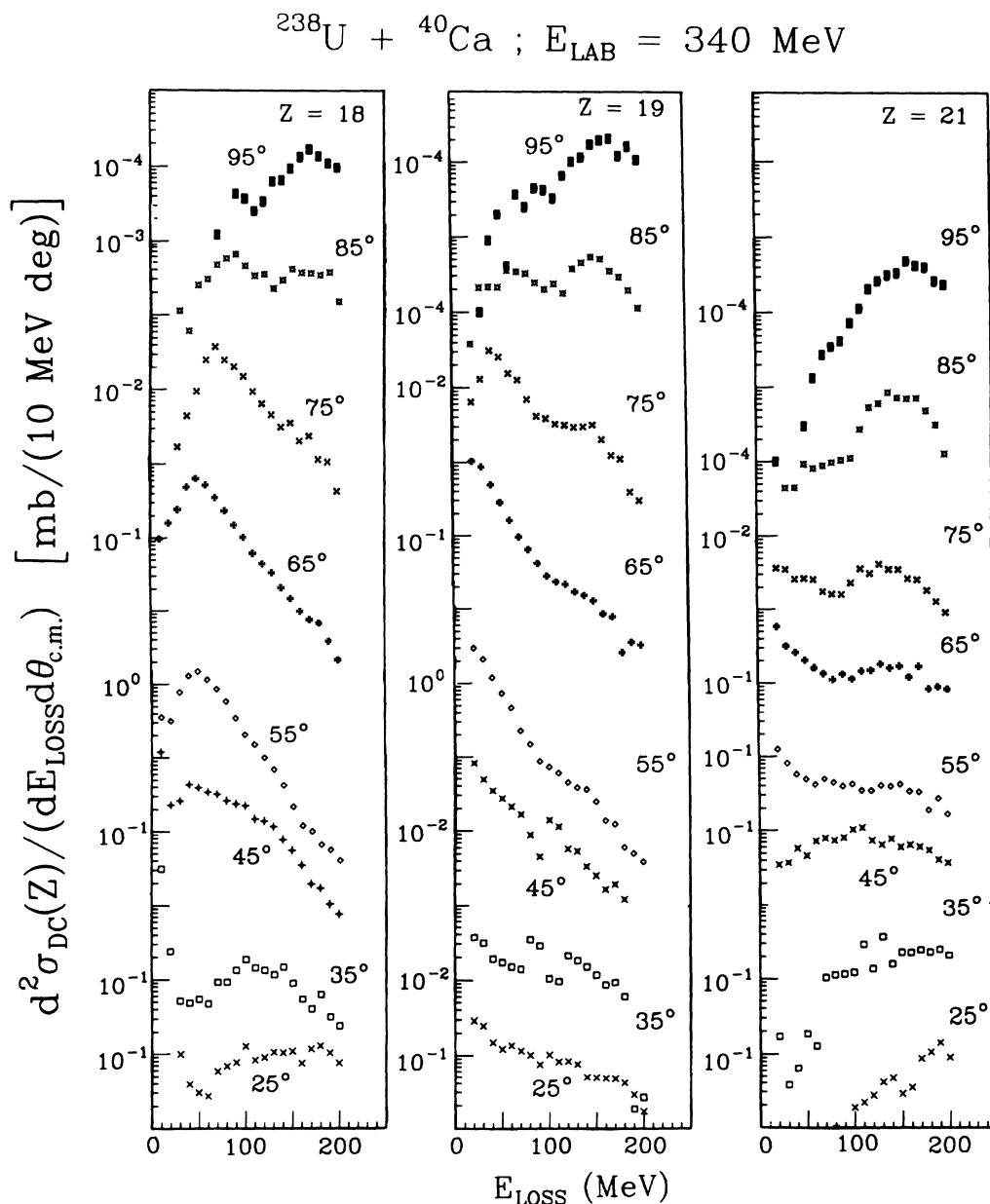

FIG. 16. Kinetic energy spectra of various elements ($Z = 18,19,21$) similar to those depicted in Fig. 15 for various center-of-mass angles.

In Randrup's dynamical reaction model the transport of mass, charge, and energy is mediated by the stochastic exchange of nucleons through the neck of the dinuclear system in the heavy ion reaction. The corresponding transport coefficients are calculated[15,16] from the instantaneous condition of the dinuclear complex, the constituents of which are always considered to be at their individual thermodynamic equilibria. The dinuclear complex can be described by a dumbell-like shape, the potential energy surface of which is illustrated in Fig. 17. The two spherical heavy ions, with radii R_P and R_T at a center separation distance of r, are connected by a cylindrical neck of variable radius ρ. The orientation angles of the fragments with respect to the beam are θ_P, θ_T, and the overall orientation of the system is given by the angle θ. Also included in this set of reaction variables is the charge Z and mass A of one of the fragments. Collectively the reaction variables are referred to as the set of generalized coordinates $\{q_i\}$. Additional variables are the nuclear temperatures of the two fragments; however, since no independent experimental information is available for these quantities, they will not be discussed in detail.

In the weak-coupling limit,[14] on which the dynamical model is based, the average values $\{\bar{q}_i,\dot{\bar{q}}_i\}$ of the macroscopic coordinates and velocities follow equations of motion described by the Lagrange-Rayleigh equations

$$\left[\frac{d}{dt}\frac{\partial}{\partial\dot{\bar{q}}_i}-\frac{\partial}{\partial\bar{q}_i}\right]L=-\frac{\partial}{\partial\dot{\bar{q}}_i}F\ , \tag{4}$$

where the index i runs over all reaction variables. The quantity $L=T-V$ is the Lagrangian and F is the Rayleigh dissipation function. The kinetic energy of the two spherical heavy ions can then be expressed as

$$T=\tfrac{1}{2}\mu[\dot{r}^2+(r\dot{\theta})^2]+\tfrac{1}{2}J_P(\dot{\theta}_P-\dot{\theta})^2+\tfrac{1}{2}J_T(\dot{\theta}_T-\dot{\theta})^2\ , \tag{5}$$

where μ is the reduced mass of the system and the moments of inertia for the fragments are given by J_i. The potential energy is described as

$$V=V_C+V_N+V_P^{LD}+V_T^{LD}-V_0\ . \tag{6}$$

In the above equation, V_C is the Coulomb potential between two spherical fragments. V_i^{LD} are the liquid-drop binding energies of the target-like and projectile-like fragments, respectively, corrected for shell effects. V_0 is a renormalization constant chosen so that $V=0$ for the configuration of a touching target-projectile combination with a center separation distance equal to their strong absorption radius. The nuclear interaction potential is calculated from the surface energy of the dinuclear system and the proximity attraction of juxtaposed surface elements of the spherical fragments outside the neck as

$$V_N(r,\rho)=-2\pi\gamma[\rho^2-\rho(l-l_{\rm geo})]$$
$$+4\pi\gamma\bar{R}b\Phi(l/b)\exp(-\rho^2/2\bar{R}b)\ . \tag{7}$$

The radius of the neck is ρ and the length of the neck l is given by

$$l=s+\frac{\rho^2}{2\bar{R}}\ . \tag{8}$$

The quantity s represents the distance between the nuclear surfaces defined by the half density radii,[14] denoted by C_P and C_T, and R is given by $C_PC_T/(C_P+C_T)$. With a surface energy parameter γ, the bracketed term in Eq. (7) describes the difference between the surface energy of two separated spherical nuclei and that of the dinuclear shape. The last term represents the proximity attraction; vanishing for large neck radii as it should, because of the increasing relative angle between the juxtaposed elements. This term is instrumental in reproducing the correct radial dependence of the proximity potential in
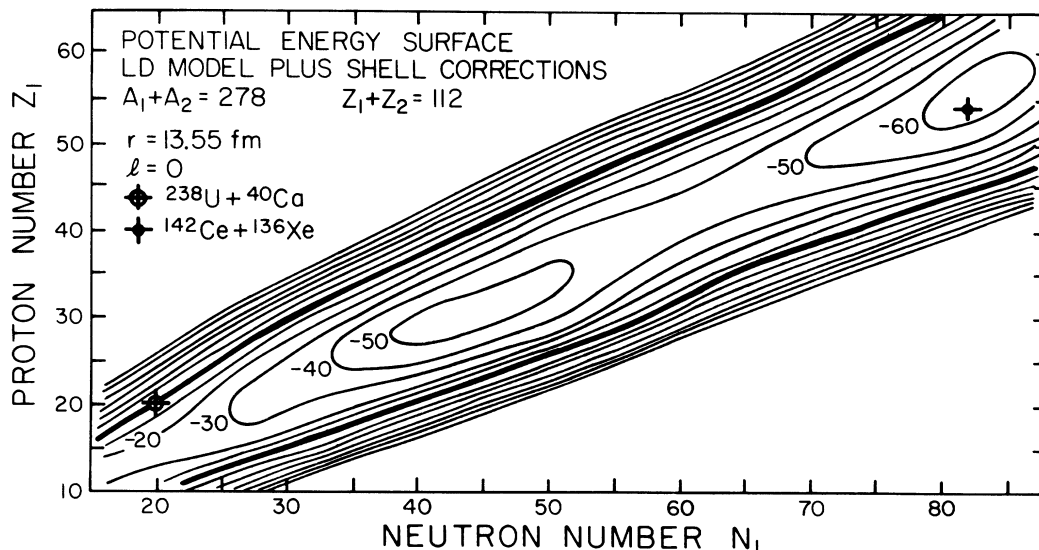

FIG. 17. Contour line representation of the liquid drop potential energy surface (with shell and proximity corrections) for all possible binary fragmentations of the composite system $A=278$, $Z=112$.

the entrance channel.[14] The quantity I_{geo} is a proximity correction[15] to account for that geometrical part of the neck area already trivially included in the proximity interaction. The proximity form factor, the reduced radius, and the surface thickness parameter are denoted by Φ, $\bar{R}$, and b, respectively.

The conversion of the kinetic energy of relative, tangential, and neck motion into intrinsic heat energy is described by the Rayleigh dissipation function F. This conversion process is mediated by the exchange of nucleons between the reaction partners ("window friction") and their collisions with the moving walls of the neck and recipient nucleus ("wall friction"). Changes in the binding energies of fragments caused by the transfer of nucleons also contribute to the dissipation of energy. Motion in the mass and charge asymmetry coordinates, as well as neck motion, are assumed to be overdamped due to the strong one-body friction forces. The dynamical driving forces for these coordinates are then determined by the balance between conservative and dissipative forces. This balance can be expressed as

$$\partial L / \partial \bar{q}_i = \partial F / \partial \dot{\bar{q}}_i . \tag{9}$$

The fluctuations in the various coordinates from the average trajectories are described in this model by a Fokker-Planck equation. The Fokker-Planck equation describing the fluctuation in neutron and proton number of one of the interaction partners can be written as

$$\frac{\partial}{\partial t}P(N,Z,t) = \left[-\frac{\partial}{\partial N}v_N - \frac{\partial}{\partial Z}v_Z \right. $$
$$\left. + \frac{\partial^2}{\partial N^2}D_{NN} + \frac{\partial^2}{\partial Z^2}D_{ZZ} \right] P(N,Z,t) . $$

$$\tag{10}$$

This equation describes the explicit time dependence of the joint probability $P(N,Z,t)$ for finding N neutrons, Z protons at time t in one of the reaction partners. Microscopic correlations between neutron and proton exchange, resulting in a finite mixed diffusion coefficient D_{NZ} have been neglected, however, those effects resulting in a global correlation between Z and N have been considered. Drift and diffusion coefficients, v and D, respectively, have been calculated microscopically by a method presented by Randrup.[15,16] These transport coefficients fulfill the generalized Einstein relation,

$$v_i = D_{ii}F_i / \tau_i^*, \quad i = N, Z \tag{11}$$

where F denotes the dynamical force driving the system along the coordinate i. The quantity τ_i^* is a measure of the energy interval about the Fermi level contributing to the exchange of nucleons.

In the numerical calculations, the drift coefficients are expanded to first order around the average trajectory as described previously.[17] The expansion procedure results in a set of coupled linear differential equations describing the motion of the first and second moments of the probability distribution P. Integration of these equations is performed along the average system trajectory. The

masses (A) and charges (Z) of the interacting fragments are adjusted at each time step in the numerical integration. The model calculations have been discussed in greater detail elsewhere.[14,17,18]

The potential surface thought to be responsible for the static driving forces present on this system is drawn in Fig. 17 for $l = 0$. The potential surface shown is a liquid drop potential surface for all binary fragmentations of the composite system with $Z = 112$ and $A = 278$. Both shell and proximity effects are included in the potential. The surface has been normalized to the entrance channel for the $^{238}U + ^{40}Ca$ system. Plotted in a contour map representation are the equipotential lines. The internuclear distance is approximated by the strong absorption radius. In addition to the global minimum at symmetry, a minimum closer to the injection point is seen. The presence of this minimum is due to the strong shell effects in the Pb region influencing the heavy partner and consequently influencing the overall potential energy. In contrast to other systems studied, the injection point lies on a very steep wall of the potential surface. The gradient of the potential energy for a trajectory with entrance channel angular momentum $l = 115\hbar$ and a total energy loss of 100 MeV is illustrated in Fig. 18 for various projectile-like fragments. As observed in this figure, the gradient is rather steep in the direction of proton loss and neutron gain by the projectile-like fragments from the $^{238}U + ^{40}Ca$ reaction.

Figure 19 depicts the mass distribution of projectile-like fragments measured at $\theta_{lab} = 44°$ with $E_{loss} = (55 \pm 5)$ MeV. The point of this figure is to illustrate that the asymmetries of the distributions are significant enough (as noted by the discrepancy between the measured distribution and the best-fit Gaussian) to warrant use of the
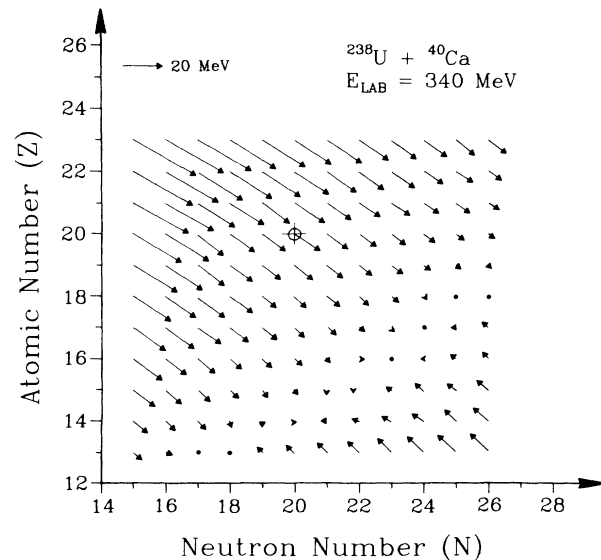

FIG. 18. Driving force $[(\Delta V / \Delta Z)^2 + (\Delta V / \Delta N)^2]^{1/2}$ for net transfer of nucleons between the projectile-like and target-like fragments. The length of each arrow denotes the magnitude of the force and the direction indicates the drift direction of the projectile-like fragment. See text.
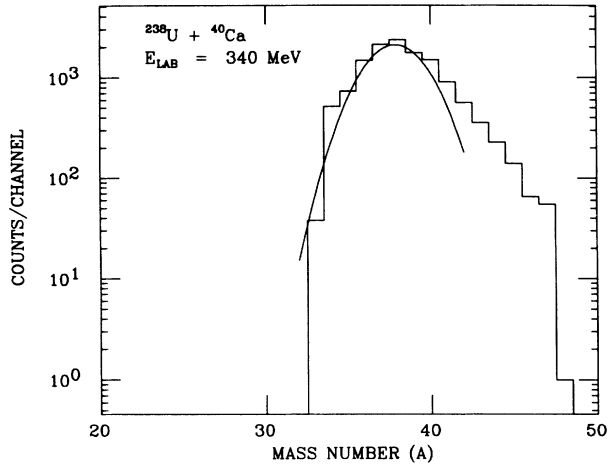
FIG. 19. Illustration of the asymmetries present in the mass degree of freedom. The histogram represents the observed mass distribution measured at $\theta_{lab} = 44°$ for $E_{loss} = 55 \pm 5$ MeV. The smooth solid line is a Gaussian fit to the experimental data.

moment approach as has previously been suggested[19] rather than by the technique of fitting the joint N-Z distribution with a two-dimensional Gaussian.[20] The first and second moments of the measured distributions are then defined in the usual fashion as

$$\langle x^n \rangle = \sum_i P(x_i) x_i^n \Big/ \sum_i P(x_i) , \qquad (12)$$

$$\sigma_x^2 = \langle x^2 \rangle - \langle x \rangle^2 , \qquad (13)$$

where P represents the intensity of a given mass or charge, and x represents the random variable (either Z or A).

Since the experimentally measured mass and charge distributions are the product distributions subsequent to particle deexcitation, they cannot be directly compared to the theoretical prediction provided by a classical trajectory reaction program. To account for the effect of particle evaporation on the reaction products, the output distributions of CLATO4 (a classical trajectory reaction code based on Randrup's model), including the predicted spin and excitation energy, have been used as the input for a statistical evaporation code PACE.[21] The output distributions of this transformation then correspond to the theoretically predicted secondary distributions which can be compared to the experimentally observed distributions. The use of CLATO4 for the above calculations of the initial partition of the total excitation energy between the two reaction fragments is justified on the basis of recent advancements in the understanding of the partitioning of excitation energy between primary fragments.[22-27] Charged-particle evaporation, although modest at most energies, is included along with neutron evaporation in calculating the effect of evaporation on the primary mass and charge distributions.

In Fig. 20, the dependence of the first and second moments of the charge distribution on increasing energy loss (corresponding to increasing interaction time) is shown as solid points. These data were measured at $\theta_{lab} = 44°$. The
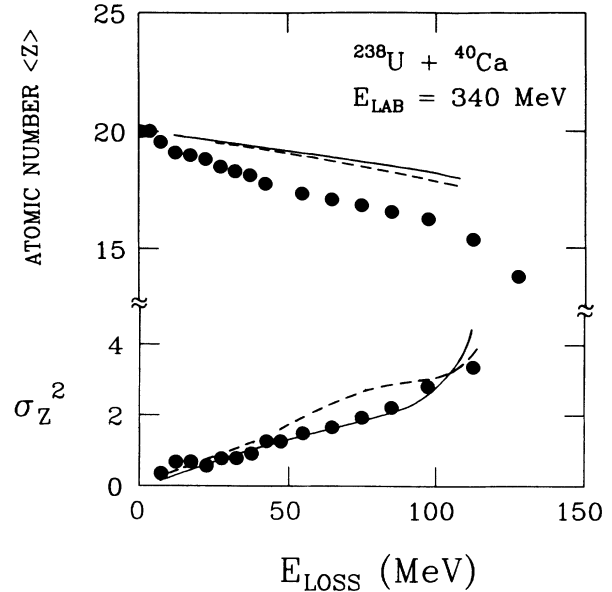

FIG. 20. Dependence of the first and second moments of the charge (Z) distribution of projectile-like fragments on the energy loss (E_{loss}). Data are represented by solid points along with the classical trajectory theoretical predictions of the primary (solid line) and secondary (dashed line) Z distributions. Data are measured at $\theta_{lab} = 44°$.

experimentally measured average charge exhibits an extremely strong drift with energy loss when compared to systems of comparable mass asymmetry. It is important to remember that the experimental drift reflects the combined effect of two different processes. The first process is the result of the proton exchange between the two heavy ions during the collision. The second process is the subsequent charged-particle evaporation from the excited primary fragments. While the particle evaporation process can only remove charge from the projectile-like fragment, the nucleon exchange process can, in principle, cause the projectile-like fragment to experience a net proton flow from the uranium-like partner. Because the effect of charged-particle evaporation is small, 0.5 unit for the highest energy losses, the drift in $\langle Z \rangle$ with increasing energy loss is a direct measure of the primary proton exchange process.

Neither the theoretically predicted primary (solid line in Fig. 20) or secondary (dashed line in Fig. 20) distributions reproduce the strong drift observed in the charge degree of freedom. The extent of the failure of the evaporation corrected theory to reproduce the first moment in charge is somewhat unusual. At an E_{loss} of 100 MeV, the corrected theory overpredicts the $\langle Z \rangle$ by about 1.7 units. This overprediction corresponds to a difference in the atomic number of the order of 10%. It is interesting to note that an earlier work[20] demonstrated the relative independence of the drift in Z to the target-projectile system for ^{56}Fe projectiles. For the systems ^{165}Ho, ^{209}Bi, and $^{238}U + ^{56}Fe$ at $E_{lab} = 462$ MeV it was found that $\langle Z \rangle$ decreases linearly as energy is dissipated

and that the decrease in $\langle Z \rangle$ for all three systems was 2.3 ± 0.1 per 100 MeV of E_{loss}, demonstrating remarkable system independence. As Fig. 20 so clearly depicts, while the decrease in $\langle Z \rangle$ is roughly linear with respect to E_{loss}, the rate is much greater than for the aforementioned systems (3.9 units in Z per 100 MeV of E_{loss}). The explanation for this stronger drift in $\langle Z \rangle$ is thought to be associated with the steeper gradient of the PES in the vicinity of the injection point for the $^{238}U + {}^{40}Ca$ reaction. The lower half of Fig. 20 portrays the relatively good agreement between the experimentally determined second moments of the charge distributions and the corresponding theoretical predictions. The theoretical predictions of the classical trajectory model are shown by the solid line. The variance corrected for particle evaporation is shown by the dashed line.

In Fig. 21 the comparison is made between the experimentally determined first and second moments (solid points) of the mass number distribution (A) and their theoretically predicted values as a function of energy loss. The data were measured at $\theta_{\text{lab}} = 44°$. While the corrected theory (dashed line) predicts an initial increase in the average mass number of the projectile-like fragment and then a leveling off or slight decrease, the experimentally measured distributions describe a rather steady decrease in the average mass number of the projectile-like fragment with increasing energy damping. The degree of the discrepancy, in this case, is an overprediction by the theory of about 4 units in $\langle A \rangle$ at an E_{loss} of 100 MeV. As seen from Fig. 20, approximately one-half of this discrepancy is associated with the failure of the theory to predict the proton drift. The experimental variances in the mass number distribution (Fig. 21, lower half) for the
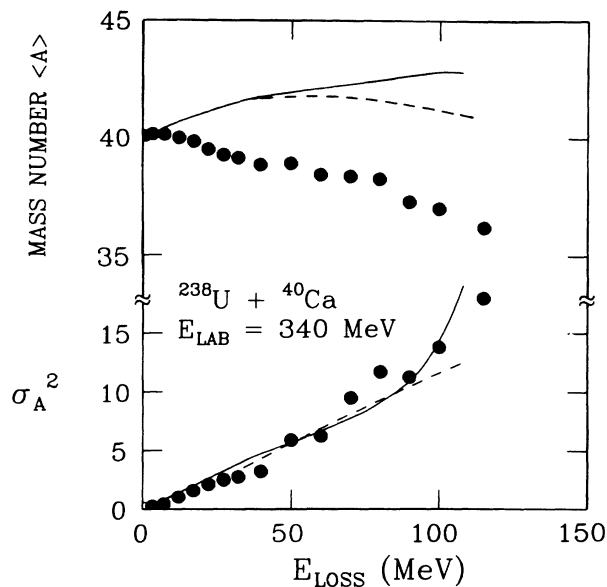
$^{238}U + {}^{40}Ca$ reaction are in good agreement with the theoretical predictions of the classical trajectory model. The solid and dashed lines represent the theoretical results before and after correction for particle emission, respectively.

In the lower part of Fig. 22 the evolution of the mass-to-charge ratio, $\langle A \rangle / \langle Z \rangle$, measured at $\theta_{\text{lab}} = 44°$, is plotted as a function of the dissipation of kinetic energy. This plot clearly demonstrates a nearly linear approach of the projectile-like fragment charge density, as a function of E_{loss}, towards a charge density near that of the composite system $(A/Z = 2.48)$. The projectile-like fragments approximately achieve equilibration of the A/Z degree of freedom as determined by the PES $(A/Z \approx 2.4)$, for the highest energy loss observed in the experiment. The theoretical prediction provides an excellent description of the equilibration of this degree of freedom. Past examination of this degree of freedom for other systems demonstrates that the good agreement achieved between theory and experiment is not unique to this case. This result is understood in terms of the relative insensitivity of the theory to the description of the evolution of $\langle A \rangle / \langle Z \rangle$. The ratio of variances, σ_A^2 / σ_Z^2, is plotted as a function of energy loss in the upper part of Fig. 22. The agreement between experiment and theory is satisfactory except at very small energy losses where contamination by elastic scattering may be important.

An extremely interesting process, the evolution of a correlation between the neutron number and the proton number, is depicted in Fig. 23. The experimental data were measured at $\theta_{\text{lab}} = 44°$. The correlation coefficient

FIG. 21. Dependence of the first and second moments of the observed mass number (A) distribution on E_{loss} (MeV) is shown by the solid points. Comparison with theoretical predictions of the primary (solid line) and secondary (dashed line) A distributions is made. Data are measured at $\theta_{\text{lab}} = 44°$.
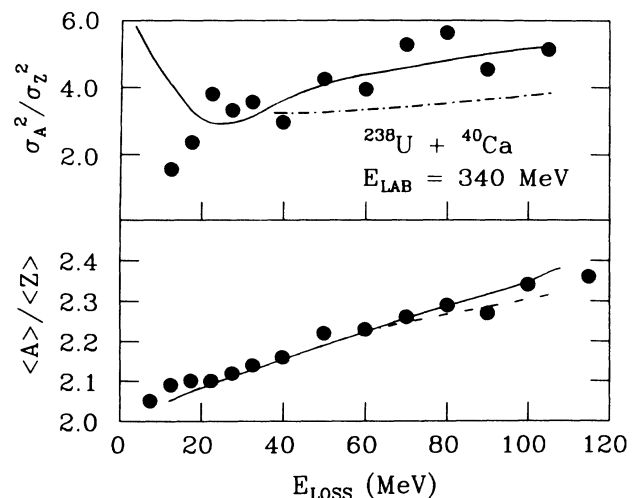

FIG. 22. Evolution of the A/Z degree of freedom with respect to the energy loss is shown in the lower part of this figure. The equilibration of the inverse charge density (A/Z) proceeds smoothly from the value of the projectile towards its global equilibrium value. Comparisons with the nucleon exchange transport reaction code are made for the primary and secondary distributions and denoted by the solid and dashed lines, respectively. The upper part of this figure shows the experimental (solid points) and theoretical (solid line) ratios of the variances σ_A^2 / σ_Z^2. All experimental data are for $\theta_{\text{lab}} = 44°$.
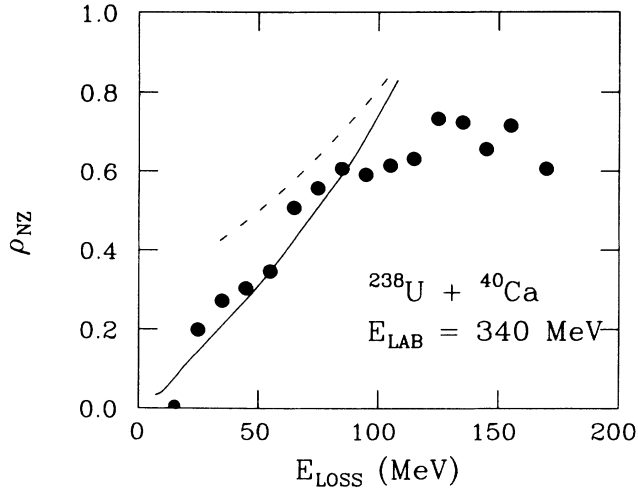
FIG. 23. Behavior of the correlation coefficient ρ_{NZ} with respect to E_{loss} (MeV). Saturative behavior predicted from the behavior of other systems is followed by the experimental data (points), however, the theoretical predictions for the primary (solid line) and secondary (dashed line) distributions fail to reproduce the saturation in the same manner as shown by the data measured at $\theta_{lab}=44°$.

ρ_{NZ} is related to the covariance of the joint $P(N,Z)$ distribution, namely,

$$\rho_{NZ} = \frac{\sigma_{NZ}}{\sigma_N \sigma_Z} \ . \qquad (14)$$

The correlation observed between the simultaneously measured A and Z distributions of the projectile-like fragments has two possible sources. The first is a correlation induced by a driving force directed to equilibrate the charge density in the stochastic nucleon exchange process. The second possibility is a correlation arising due to the effect of the alignment of the beta-stable valley on the fragment deexcitation process. For mass asymmetric systems, previous studies[14,28] have estimated the effect of evaporative cooling on the two-dimensional joint probability distribution $P(N,Z)$. In the case of ^{165}Ho + ^{56}Fe at $E_{lab}=465$ MeV, the joint probability distribution $P(N,Z)$ rotates and broadens disproportionately in the particle deexcitation process, yet nevertheless, the observed correlation has a substantial degree of correlation arising from the nucleon exchange process and is not simply an artifact created by the particle evaporation. Similar arguments can be made in the present case of the ^{238}U + ^{40}Ca system, illustrated in Fig. 23 showing the effect of the evaporation (dashed line) on the predicted correlation of the primary distribution (solid line). However, for large energy losses (> 80 MeV), the theory overpredicts somewhat the degree of correlation of the observed distribution. The reason for this discrepancy may be related to the overprediction of the variances of the atomic and mass number distributions by the theory at the higher energy losses.

In order to determine whether the behavior of the variances contains any correlations, it is instructive to exam-

ine Fig. 24. In this figure, the variances in the mass distribution gated on different Z's (isotopic variances) from $Z = 14$ to $Z = 19$ are plotted for $\theta_{lab}=44°$. It is exceedingly interesting to note that the saturative behavior expected from the study of other systems[14] is reproduced for this system. The saturation of the marginal variance in A for given Z demonstrates the fact that the A distribution is correlated to the Z on which the gate is set and naturally cannot grow in unbounded fashion but must manifest the topology of the PES. The absence of data, at small energy losses, for the Z's far from the projectile Z is the result of a secondary relationship between $(Z - Z_p)$ and the interaction time which for these Z values requires a greater exploration of the topology of the potential surface by the system.

The average behavior of the isotopic variance as a function of E_{loss} is illustrated in Fig. 25 for atomic num-
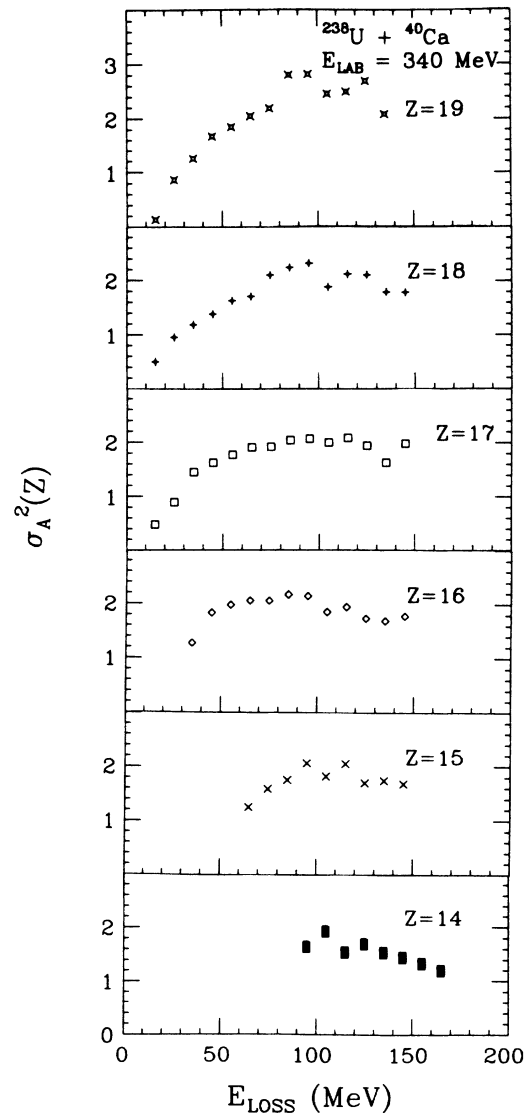

FIG. 24. Isotopic variances (variance in the A distribution for fixed Z) for various elements ($Z = 14$–19) are shown as a function of E_{loss} (MeV). Data are measured at $\theta_{lab}=44°$.
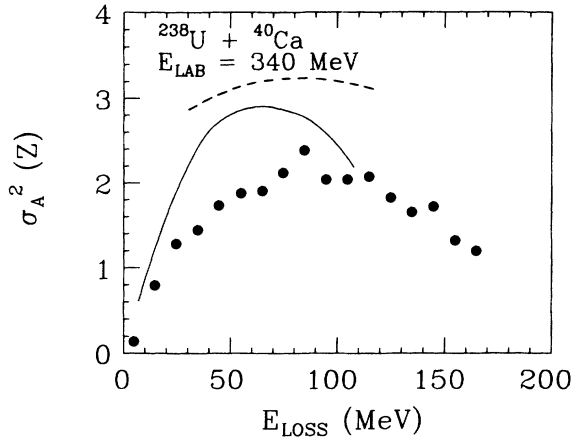
FIG. 25. The evolution of the isotopic variance, averaged over several Z bins ($Z = 14-19$), is shown as a function of increasing energy loss (E_{loss}). Data, measured at $\theta_{lab} = 44°$, are represented by the points while the theoretical behavior of this quantity for the primary and secondary distributions are illustrated by the solid and dashed lines, respectively.

FIG. 26. Isobaric variance (variance in the Z distribution for fixed A) evolution with increasing energy loss (E_{loss}) is shown averaged over several A bins ($A = 34-42$). Data, measured at $\theta_{lab} = 44°$, are represented by the points while the theoretical behavior of this quantity for the primary and secondary distributions of reaction products are illustrated by the solid and dashed lines, respectively.

bers $14 < Z < 19$. The solid line gives the theoretical result for the conditional mass variance of the primary distribution. The effect of evaporation on the unconditional variances, is shown by the dashed curve. As can be seen, the theory predicts larger isotopic variances than those observed. It is worthwhile to note that the experimental isotopic variances are comparable to those measured for the ^{165}Ho + ^{56}Fe system.[22] The implication of the similar variances in the isotopic distributions is that the forces restoring excursions perpendicular to the restriction of constant Z are similar for the ^{238}U + ^{40}Ca system. Such detailed knowledge, concerning the topology of the PES governing the evolution of the system, is vital to a more comprehensive understanding of the nucleon exchange process.

Figure 26 illustrates the dependence of the isobaric variance (second moment of the Z distribution for fixed A) on energy loss for $\theta_{lab} = 44°$. This figure provides a complement to the isotopic variance shown previously. Examination of both isotopic and isobaric variances present more detailed information about the evolution of the two-dimensional joint probability distribution in the (A,Z) plane. A comparison of the measured isobaric variances with measured isotopic variances yields information concerning the curvature of the PES in the A and Z degrees of freedom. Narrower isobaric distributions indicate that the PES has stronger restoring forces (more curvature) in the charge (Z) degree of freedom than in the mass number (A) degree of freedom. In addition, comparison of the magnitude of the saturation value of the isobaric variance for this system as compared to ^{238}U + ^{56}Fe and ^{165}Ho + ^{56}Fe reactions at $E_{lab} = 465$ MeV shows that while the latter systems saturate at slightly larger values (0.6 and 0.8, respectively), the present system shows a similar behavior. The theoretical predictions of the primary isobaric variances and those corrected for particle evaporation are shown by the solid
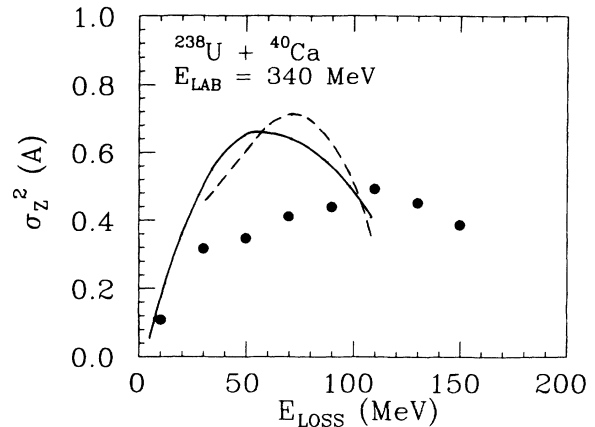
and dashed lines, respectively. The agreement between theory and experiment is rather poor.

From the previous discussion of the mass, charge, and energy transfer, it can be surmised that while the system ^{238}U + ^{40}Ca at $E_{lab} = 340$ MeV exhibits several general features already elucidated in previous studies of mass and charge transfer in strongly damped collisions, this system also demonstrates its rather unique character in several distinct ways. Discrepancies between theory and experimental observation appear to be accentuated for this system. While a qualitative understanding is possible in terms of the unique nature of the PES and the extremely large neutron excess of the heavy reaction partner, a more satisfactory quantitative understanding still needs to be achieved.

V. CONCLUSIONS

The damped reaction ^{238}U + ^{40}Ca at $E_{lab} = 340$ MeV has provided a unique opportunity both to study the general features of an extremely mass-asymmetric system and to test the predictive power of current nucleon transport theories for a system where the static driving forces are unusually large. The angular distributions ($d\sigma_{DC}/d\theta$ vs θ) of the damped reaction fragments exhibit a classic case of orbiting. Despite the neutron-richness of uranium and neutron pick-up by the projectile-like fragment, the distribution of all projectile-like products was found to lie within the (Z, A) region of already known nuclides. The underlying reason for this is no doubt the neutron deficiency of the ^{40}Ca projectile. Symmetry of the mass distribution for various elements (with respect to a Gaussian shape) was found to increase as one progressed away from the projectile Z. This behavior suggests that fluctuations in the mass degree of freedom become sufficient to eliminate asymmetries for long interaction

times. The exception to this rule of asymmetry in mass for Z's close to the projectile Z was the symmetry found in the mass distribution for $Z = 21$ and $Z = 22$. In addition, the diffusion plot (Fig. 12) revealed that the intensity for all Z's > 20 did not evolve from the elastic peak in the same manner as the intensity for all Z's < 20. A large amount of kinetic energy must be dissipated before net proton transfer to the projectile-like fragment occurs. The presence of Z's > 20 at energies close to and centered about the kinetic energy predicted from systematics of fully relaxed fragments raises the question of the degree of contamination of strongly damped events in this Z range with a contribution from an intermediate reaction process.

The asymmetries present in the mass and charge distributions that were measured with high resolution precluded the extraction of moments from the joint A-Z distributions by a Gaussian fit technique,[20] requiring instead a direct application of the moment approach.[19] Contrary to previous measurements, the rate of drift in Z with energy loss was found to be substantially larger than for systems of similar mass asymmetry and total mass. This effect was ascribed to the large gradient of the PES in the neighborhood of the injection point. The observed distributions were also compared with the distributions predicted by a nucleon exchange model subsequent to the application of an appropriate evaporation calculation. Poor prediction by the model of the experimentally measured drifts was found. This discrepancy in the moments of the Z and A distributions as a function of E_{loss} is perhaps a failure of the model to correctly account for the steep gradient of the PES for this system. On the other hand, the model predicts the variances in atomic and mass number distributions reasonably well as a function of E_{loss}. It has also been established that the projectile-like fragments approximately achieve equilibration of the N/Z degree of freedom, as determined by the local PES,

for the highest energy losses. Examination of the correlation coefficient afforded an opportunity to estimate the degree of correlation present in the stochastic nucleon exchange process. It was found that the nucleon exchange transport process is responsible for most of the correlation present in the observed distribution $P(N,Z)$. For large energy losses, however, it has been shown[14] that the correlation induced by the particle deexcitation process increases. Comparison of the experimentally measured isotopic and isobaric variances with theory reveal that while the experimental widths show the saturative behavior observed experimentally in other systems, the theoretical predictions are in poor agreement with the data suggesting insufficient detailed knowledge of the static driving force affecting the evolution of the system.

While some of the results from this system have been surprising, in some aspects differing from other systems studied, its full impact will hopefully be better understood in the context of a more comprehensive comparison of the present reaction with the reaction $^{238}U + {}^{48}Ca$ at $E_{lab} = 410$ MeV and the reaction $^{238}U + {}^{40}Ca$ at a lower energy of $E_{lab} = 260$ MeV. The balance between dynamical and static driving forces and the true role of the PES of the dinuclear complex in governing the mass, charge, and energy of the projectile-like fragment must be better determined if the underlying microscopic mechanism of .dissipative heavy-ion collisions is to be understood.

[1]H. Breuer, A. Gökmen, C. J. Kulesza, G. Lavelle, A. C. Mignerey, K. K. Kwiatkowski, V. E. Viola, J. R. Birkelund, A. D. Hoover, J. R. Huizenga, W. U. Schröder, W. W. Wilcke, H. J. Wollersheim, R. R. Betts, B. G. Glagola, C. Davids, and K. L. Wolf, Workshop on Nuclear Dynamics III, Copper Mountain, Colorado, March 1984.

[2]W. U. Schröder, J. R. Birkelund, J. R. Huizenga, K. L. Wolf, and V. E. Viola, Jr., Phys. Rep. 45, 301 (1978).

[3]K. Braune, thesis, Max-Planck-Institut, Heidelberg, 1978 (unpublished); D. Schwalm (private communication).

[4]D. Schwalm, A. Bamberger, P. G. Bizetti, B. Povh, G. A. P. Englebertink, J. W. Olness, and E. K. Warburton, Nucl. Phys. A192, 449 (1972).

[5]K. Warburton, J. W. Olness, and A. R. Poletti, Phys. Rev. 160, 938 (1967).

[6]H. J. Wollersheim, W. W. Wilcke, J. R. Birkelund, J. R. Huizenga, and W. U. Schröder, Phys. Rev. C 24, 2114 (1981).

[7]J. B. Moulton, J. E. Stephenson, R. P. Schmitt, and G. Wozniak, Nucl. Instrum. Methods 157, 325 (1978).

[8]W. E. Frahn and R. H. Venter, Ann. Phys. (N.Y.) 24, 243

(1963); W. E. Frahn, Phys. Rev. Lett. 26, 568 (1971); Ann. Phys. (N.Y.) 72, 524 (1972).

[9]W. E. Frahn, Nucl. Phys. A302, 267 (1978).

[10]R. T. de Souza, W. U. Schröder, J. R. Huizenga, J. Tōke, S. S. Datta, and I. M. Govil (unpublished).

[11]A. G. Artukh, V. B. Avdeichikov, G. S. Gridneev, V. L. Mikheev, V. V. Volkov, and J. Wilczynski, Nucl. Phys. A176, 284 (1971).

[12]M. A. Butler, S. S. Datta, R. T. de Souza, J. R. Huizenga, W. U. Schröder, J. Tōke, and J. L. Wile, Phys. Rev. C 34, 2016 (1986).

[13]A. G. Artukh, G. F. Gridnev, V. L. Mikheev, V. V. Volkov, and J. Wilczynski, Nucl. Phys. A215, 91 (1973).

[14]W. U. Schröder and J. R. Huizenga, in Damped Nuclear Reactions, Vol. 2 of Treatise on Heavy-Ion Science, edited by D. A. Bromley (Plenum, New York, 1984), Chap. 3, and references cited therein.

[15]J. Randrup, Nucl. Phys. A307, 319 (1978); A327, 490 (1979); A383, 468 (1982).

[16]T. Døssing and J. Randrup, Nucl. Phys. A433, 215 (1985);

A433, 280 (1985).

[17]W. U. Schröder, J. R. Huizenga, and J. Randrup, Phys. Lett. **98B**, 355 (1981).

[18]W. U. Schröder, R. T. de Souza, J. R. Huizenga, and L. M. Schmieder, Proceedings of the International Symposium on Nuclear Fission and Heavy-Ion Reactions [Nucl. Sci. Res. Conf. Series, **11**, 255 (1987)].

[19]H. Freiesleben and J. V. Kratz, Phys. Rep. **106**, 1 (1984).

[20]H. Breuer, A. C. Mignerey, V. E. Viola, K. L. Wolf, J. R. Birkelund, D. Hilscher, J. R. Huizenga, W. U. Schröder, and W. W. Wilcke, Phys. Rev. C **28**, 1080 (1983).

[21]A. Gavron, Phys. Rev. C **21**, 230 (1980).

[22]J. R. Huizenga, W. U. Schröder, J. R. Birkelund, and W. W. Wilcke, Nucl. Phys. **A387**, 257c (1982).

[23]T. C. Awes, R. L. Ferguson, R. Novotny, F. E. Obenshain, F. Plasil, S. Pontoppidan, V. Rauch, G. R. Young, and H. Sann, Phys. Rev. Lett. **52**, 251 (1984).

[24]R. Vandenbosch, A. Lazzarini, D. Leach, D. K. Lock, A. Ray, and A. Seamster, Phys. Rev. Lett. **52**, 1964 (1984).

[25]H. Sohlbach, H. Freiesleben, P. Braun-Munzinger, W. F. W. Schneider, D. Schull, B. Kohlmeyer, M. Marinescu, and F. Pühlhofer, Phys. Lett. **153B**, 386 (1985).

[26]J. L. Wile, W. U. Schröder, J. R. Huizenga, and D. Hilscher, Phys. Rev. C **35**, 1608 (1987).

[27]D. R. Benton, H. Breuer, F. Khazaie, K. Kwiatkowski, V. E. Viola, S. Bradley, A. C. Mignerey, A. P. Weston-Dawkes, and R. J. McDonald, Phys. Lett. **185B**, 326 (1987).

[28]D. K. Lock, R. Vandenbosch, and J. R. Randrup, Phys. Rev. C **31**, 1268 (1985).